Website: http://AIMsciences.org pp. **659-686** 

## MULTIRESOLUTION ANALYSIS FOR 2D TURBULENCE. PART 1: WAVELETS VS COSINE PACKETS, A COMPARATIVE STUDY

P. Fischer

M. A. B. University of Bordeaux 1 33405 Talence Cedex, France

(Communicated by K.K. Tung)

ABSTRACT. The widely accepted theory of two-dimensional turbulence predicts a direct downscale enstrophy cascade with an energy spectrum behaving like  $k^{-3}$  and an inverse upscale energy cascade with a  $k^{-5/3}$  decay. Nevertheless, this theory is in fact an idealization valid only in an infinite domain in the limit of infinite Reynolds numbers, and is almost impossible to reproduce numerically. A more complete theoretical framework for the two-dimensional turbulence has been recently proposed by Tung  $et\ al.$  This theory seems to be more consistent with experimental observations, and numerical simulations than the classical one developed by Kraichnan, Leith and Batchelor.

Multiresolution methods like the wavelet packets or the cosine packets, well known in signal decomposition, can be used for the 2D turbulence analysis. Wavelet or cosine decompositions are more and more used in physical applications and in particular in fluid mechanics. Following the works of M. Farge et al, we present a numerical and qualitative study of a two-dimensional turbulence fluid using these methods. The decompositions allow to separate the fluid in two parts which are analyzed and the corresponding energy spectra are computed. In the first part of this paper, the methods are presented and the numerical results are briefly compared to the theoretical spectra predicted by the both theories. A more detailed study, using only wavelet packets decompositions and based on numerical and experimental data, will be carried out and the results will be reported in the second part of the paper. A tentative of physical interpretation of the different components of the flow will be also proposed.

1. **Introduction.** The application of wavelets to fluid dynamics have been the topic of many papers, published since 1992, and many of them by Farge *et al* [16, 17, 18] <sup>1</sup>. The main idea developed in these papers is that the vorticity field of a turbulent flow can be easily decomposed in coherent and incoherent parts thanks to an orthogonal wavelet decomposition. The coherent part, corresponding to the strongest wavelet coefficients, is in fact composed by vortices and the so-called incoherent part, corresponding to the weakest coefficients, is mainly composed by vorticity filaments. In the present paper, the computations have been performed from vorticity and velocity fields obtained from two Numerical Simulations. These

 $<sup>2000\</sup> Mathematics\ Subject\ Classification.\ 65T60, 76F65.$ 

Key words and phrases. Wavelets, 2D turbulence.

<sup>&</sup>lt;sup>1</sup>see also the web page of M. Farge http://wavelets.ens.fr/PUBLICATIONS/publications.htm

experiments are based on a two-dimensional channel flow perturbed by an horizontal array of five cylinders. They will be briefly described in the seguel but the details can be found in [8, 9].

- 2. Wavelet and Cosine packets decompositions. Wavelet packets are generalizations of the classical orthogonal compactly-supported wavelets, and cosine packets generalizations of the Discrete Cosine Transform. One will first introduce the one-dimensional wavelet packets theory, and then extend it to higher dimension. The Best Basis algorithm will be described in the last section of this part following the review on the cosine packets method.
- 2.1. One-dimensional wavelet bases. The theoretical construction of orthogonal wavelet families is intimately related to the notion of Multiresolution Analysis [28]. A Multiresolution Analysis is a decomposition of the Hilbert space  $L^2(\mathbb{R})$ of physically admissible functions (i.e square integrable functions) into a chain of closed subspaces,

$$\ldots \subset V_2 \subset V_1 \subset V_0 \subset V_{-1} \subset V_{-2} \ldots$$

- $\bigcap_{j \in \mathbb{Z}} V_j = \{0\}$  and  $\bigcup_{j \in \mathbb{Z}} V_j$  is dense in  $L^2(\mathbb{R})$   $f(x) \in V_j \Leftrightarrow f(2x) \in V_{j-1}$
- $f(x) \in V_0 \Leftrightarrow f(x-k) \in V_0$
- There is a function  $\varphi \in V_0$ , called the father wavelet, such that  $\{\varphi(x-k)\}_{k\in\mathbb{Z}}$ is an orthonormal basis of  $V_0$

Let  $W_j$  be the orthogonal complementary subspace of  $V_j$  in  $V_{j-1}$ :

$$V_j \oplus W_j = V_{j-1} \tag{1}$$

This space contains the difference in information between  $V_j$  and  $V_{j-1}$ , and allows the decomposition of  $L^2(\mathbb{R})$  as a direct form:

$$L^2(\mathbb{R}) = \bigoplus_{j \in \mathbb{Z}} W_j \tag{2}$$

Then, there exists a function  $\psi \in W_0$ , called the mother wavelet, such that  $\{\psi(x - y)\}$  $\{k\}_{k\in\mathbb{Z}}$  is an orthonormal basis of  $W_0$ . The corresponding wavelet bases are then characterized by:

$$\varphi_{j,k}(x) = 2^{-j/2} \varphi(2^{-j}x - k), \quad k, j \in \mathbb{Z},$$
 (3)

$$\psi_{j,k}(x) = 2^{-j/2}\psi(2^{-j}x - k), \quad k, j \in \mathbb{Z}.$$
 (4)

The mother wavelet corresponding to the chosen wavelet basis verifies:

$$\int_{\mathbb{R}} dx \, \psi(x) \, x^m = 0, \quad m = 0, \dots, M - 1 \,\,, \tag{5}$$

which means that it has M vanishing moments.

Since the scaling function  $\varphi(x)$ , and the mother wavelet  $\psi(x)$  belong to  $V_{-1}$ , they admit the following expansions:

$$\varphi(x) = \sqrt{2} \sum_{k=0}^{L-1} h_k \, \varphi(2x - k), \quad h_k = \langle \varphi, \varphi_{-1,k} \rangle , \qquad (6)$$

$$\psi(x) = \sqrt{2} \sum_{k=0}^{L-1} g_k \, \varphi(2x - k), \quad g_k = (-1)^k h_{L-k-1} \,, \tag{7}$$

where the number L of coefficients is connected to the number M of vanishing moments and is also connected to other properties that can be imposed to  $\varphi(x)$ . The families  $\{h_k\}$  and  $\{g_k\}$  form in fact a conjugate pair of quadrature filters H and G. Functions verifying (6) or (7) have their support included in  $[0, \ldots, L-1]$ . Furthermore, if there exists a coarsest scale, j=n, and a finest one, j=0, the bases can be rewritten as:

$$\varphi_{j,k}(x) = \sum_{l=0}^{L-1} h_l \, \varphi_{j-1,2k+l}(x), \quad j = 1, \dots, n,$$
(8)

and

$$\psi_{j,k}(x) = \sum_{l=0}^{L-1} g_l \, \varphi_{j-1,2k+l}(x), \quad j = 1, \dots, n .$$
 (9)

The wavelet transform of a function f(x) is then given by two sets of coefficients defined as

$$d_k^j = \int_{\mathbb{R}} dx f(x) \psi_{j,k}(x) , \qquad (10)$$

and

$$r_k^j = \int_{\mathbb{R}} dx \, f(x) \, \varphi_{j,k}(x) \ . \tag{11}$$

Starting with an initial set of coefficients  $r_k^0$ , and using (8) and (9), coefficients  $d_k^j$  and  $r_k^j$  can be computed by means of the following recursive relations:

$$d_k^j = \sum_{l=0}^{L-1} g_l \, r_{2k+l}^{j-1} \,, \tag{12}$$

and

$$r_k^j = \sum_{l=0}^{L-1} h_l \, r_{2k+l}^{j-1} \ . \tag{13}$$

Coefficients  $d_k^j$ , and  $r_k^j$  are considered in (12) and (13) as periodic sequences with the period  $2^{n-j}$ . The set  $d_k^j$ , is composed by coefficients corresponding to the decomposition of f(x) on the basis  $\psi_{j,k}$  and  $r_k^j$  may be interpreted as the set of averages at various scales.

2.2. One-dimensional wavelet packets. Let H and G be a conjugate pair of quadrature filters whose the coefficients are respectively denoted by  $h_j$  and  $g_j$ . One denotes by  $\psi_0$  and  $\psi_1$  the corresponding father and mother wavelets. The following sequence of functions can be defined using the filters H and G:

$$\psi_{2n}(x) = \sqrt{2} \sum_{j \in \mathbb{Z}} h_j \psi_n(2x - j), 
\psi_{2n+1}(x) = \sqrt{2} \sum_{j \in \mathbb{Z}} g_j \psi_n(2x - j).$$
(14)

The set of these functions  $\{\psi_n\}_n$  defines the wavelet packets associated to H and G. An orthonormal wavelet packet basis of  $L^2(\mathbb{R})$  is any orthonormal basis selected from among the functions  $2^{s/2}\psi_n(2^sx-j)$ . The selection process, the so-called Best Basis algorithm, will be described in the sequel. Each basis element is characterized by three parameters: scale s, wavenumber s and position s. A useful representation of the set of wavelet packet coefficients is that of a rectangle of dyadic blocks. For instance, if one considers a signal defined at 8 points s, then the wavelet packet coefficients of this function can be summarized by Table 1.

| $x_1$   | $x_2$   | $x_3$   | $x_4$   | $x_5$   | $x_6$   | $x_7$   | $x_8$   |
|---------|---------|---------|---------|---------|---------|---------|---------|
| $r_1$   | $r_2$   | $r_3$   | $r_4$   | $d_1$   | $d_2$   | $d_3$   | $d_4$   |
| $rr_1$  | $rr_2$  | $dr_1$  | $dr_2$  | $rd_1$  | $rd_2$  | $dd_1$  | $dd_2$  |
| $rrr_1$ | $drr_1$ | $rdr_1$ | $ddr_1$ | $rrd_1$ | $drd_1$ | $rdd_1$ | $ddd_1$ |

Table 1. Dyadic blocks of wavelet packet coefficients

Each row is obtained by the application of either filter H or G to the previous row. The application of H is denoted by r as "resuming" and the application of G by d as "differencing". For instance, the set  $\{rd_1 \ rd_2\}$  is obtained by the application of the filter H to  $\{d_1 \ d_2 \ d_3 \ d_4\}$ , and  $\{dd_1 \ dd_2\}$  by the application of the filter G. The so called Daubechies wavelets defined in [14] with several numbers of vanishing moments have been used in the sequel.

2.3. One-dimensional Cosine packets. Many papers dealing with the design of orthonormal bases built from an overlapping bell and a Fourier-like transform has been published during the last few years [1], [4], [29], [30]. The family of local cosine basis functions chosen in this paper can be written as:

$$W_{k,n}(x) = b_k(x)\cos((n+\frac{1}{2})\pi x)$$
(15)

where the function  $b_k$  is a smooth window. We briefly review here the construction of the family of basis functions. Let  $\bigcup_{k=-\infty}^{k=+\infty}[x_k,x_{k+1}]$  be a cover of  $\mathbb R$ . We define a neighborhood around each point  $x_k:[x_k-\epsilon,x_k+\epsilon]$  such that  $x_k-\epsilon< x_k< x_k+\epsilon \le x_{k+1}-\epsilon$ . Then the bells  $b_k$  verify:

$$\forall x \in [x_k - \epsilon, x_k + \epsilon], \quad b_k(x)b_{k-1}(2x_k - x) + b_k(2x_k - x)b_{k-1}(x) \neq 0 \tag{16}$$

and

$$\forall x \in [x_k + \epsilon, x_{k+1} - \epsilon], \quad b_k(x) \neq 0. \tag{17}$$

These special properties insure orthogonality. The local cosine functions are then defined as:

$$\psi_{k,n}(x) = b_k(x)C_{k,n}(x) \tag{18}$$

where  $C_{k,n}(x)$  is the family of basis functions of the DCT-IV:

$$C_{k,n}(x) = \sqrt{\frac{2}{x_{k+1} - x_k}} \cos\left(\left(n + \frac{1}{2}\right)\pi \frac{x - x_k}{x_{k+1} - x_k}\right). \tag{19}$$

Depending on the choice for the bells  $b_k$ , different sets of basis functions can be defined. The bell function chosen for the computation in the sequel is the simple positive lobe of a sine function.

A multiscale version of the local cosine bases can be designed using dyadic partitions of  $\mathbb{R}$ . Like the one-dimensional wavelet packets, the set of cosine packets contains atoms that can be characterized by scale s, wavenumber n and position k. The scale s will be connected to the bell size, the wavenumber n to the frequency index, and the position k to the left endpoint of the bell:

$$\psi_{snk}(x) = \sqrt{\frac{2}{2^s}} \quad b_k\left(\frac{x}{2^s}\right)\cos\left((n+\frac{1}{2})\pi\frac{x-x_k}{2^s}\right) \tag{20}$$

The cosine packet coefficients can also be described by a rectangle of dyadic blocks (as in Table 1) where each block corresponds to a bell in a given scale (1 row = 1 scale).

- 2.4. **Two-dimensional packets.** Two-dimensional wavelet or cosine packets can be obtained by tensor products  $\psi_{snk}(x).\psi_{s'n'k'}(y)$  of one-dimensional basis elements. The support of these functions is exactly the cartesian product of the supports of  $\psi_{snk}(x)$  and  $\psi_{s'n'k'}(y)$ . The same scale s=s' will be used in the sequel. Subsets of such functions can be indexed by dyadic squares, with the squares corresponding to the nominal supports of the functions in the cosine packets case, and to the application of one of the following filters  $H \otimes H = H_x H_y$ ,  $H \otimes G = H_x G_y$ ,  $G \otimes H = G_x H_y$ , or  $G \otimes G = G_x G_y$  for the wavelet packets case. A graphical representation of a two-dimensional wavelet packets decomposition is given in Figure 1.
- 2.5. Best basis algorithm. Arrays of wavelet and cosine packets constitute huge collections of basis from which one has to choose and pick. The main criterion consists in seeking a basis in which the coefficients, when rearranged into decreasing order, decrease as fast as possible. Several numerical criteria do exist and one refers to [36] for more details. The *entropy* has been chosen since it is the more often used for this type of application. For a given one-dimensional vector  $u = \{u_k\}$ , it is defined as:

$$E(u) = \sum_{k} p(k) \log(\frac{1}{p(k)}), \tag{21}$$

where  $p(k) = \frac{|u_k|^2}{\|u\|^2}$  is the normalized energy of the  $k^{\text{th}}$  element of the vector under study. If p(k) = 0 then we set  $p(k)\log(\frac{1}{p(k)}) = 0$ . All the terms in the sum are positive. In fact, the entropy measures the logarithm of the number of meaningful coefficients in the original signal. The vector  $p = \{p(k)\}_k$  can be seen as a discrete probability distribution function since  $0 \le p(k) \le 1$ ,  $\forall k$  and  $\sum_k p(k) = 1$ . It can be easily shown that if only N of the values p(k) are nonzero, then  $E(u) \leq \log N$ . Such a probability distribution function is said to be concentrated into at most Nvalues. If E(u) is small then we may conclude that u is concentrated into a few values of p(k), with all other values being rare. The overabundant set of coefficients is naturally organized into a quadtree of subspaces by frequency. Every connected subtree containing the root corresponds to a different orthonormal basis. The most efficient of all the bases in the set may be found by recursive comparison: the choice algorithm will find the global minimum in O(N) operations, where N is the initial degree of freedom number. In fact, the basis is chosen automatically to best represent the original data. Hence the name best basis. Routines in Matlab written by D. Donoho [15] and based on the algorithms designed by M.V. Wickerhauser are used for performing the packets decompositions and for searching for the best bases.

## 3. Experimental setup.

3.1. **General description.** Two numerical experiments have been performed. Both of them consist in the numerical simulation of a two-dimensional channel flow perturbed by an horizontal array of five cylinders, as on Figure 2. The length of the channel  $\Omega$  is four times its width L; the Reynolds number based on the cylinders diameter (equal to  $0.1 \times L$ ) is Re = 50000.

The first experiment consists in solving numerically the NS/Brinkman model which is described in section 3.2,  $\Omega$  being the rectangular channel,  $\Omega_s$  (the "obstacle" subset) being the union of the five disks corresponding to the five cylinders and  $\Omega_f$ 

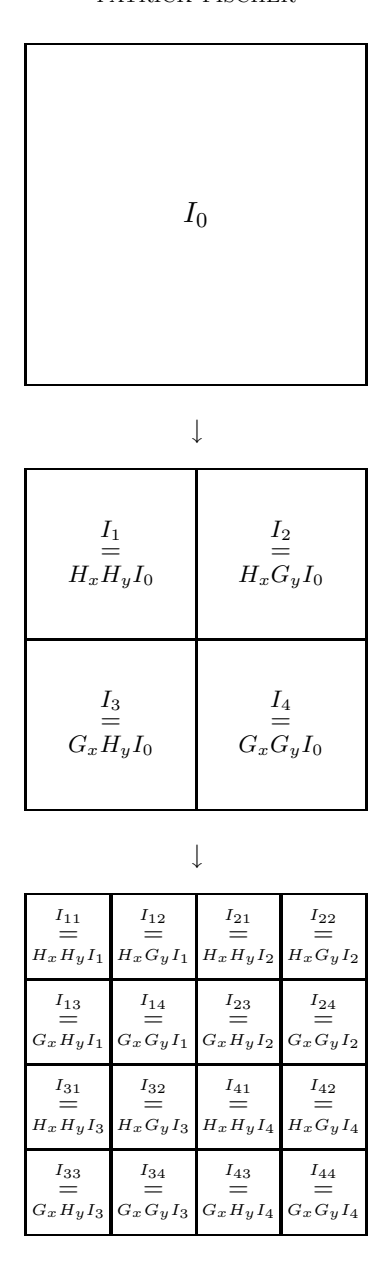


FIGURE 1. Two levels of two dimensional wavelet packets decomposition

being the fluid domain. This experiment is referred as simulation I. In the second experiment (which also consists in solving numerically the NS/Brinkman model as described precisely in section 3.2, with the same boundary data as in simulation I), the "obstacle" set  $\Omega_s$  is the union of the five horizontal disks together with 18 small disks (with diameter equal to  $0.05 \times L$ ) lying symmetrically along the vertical edges of the channel, as shown on Figure 2. In this second experiment (denoted as simulation II), additional disks (corresponding to additional cylinders) have been added in order to increase the number of merging

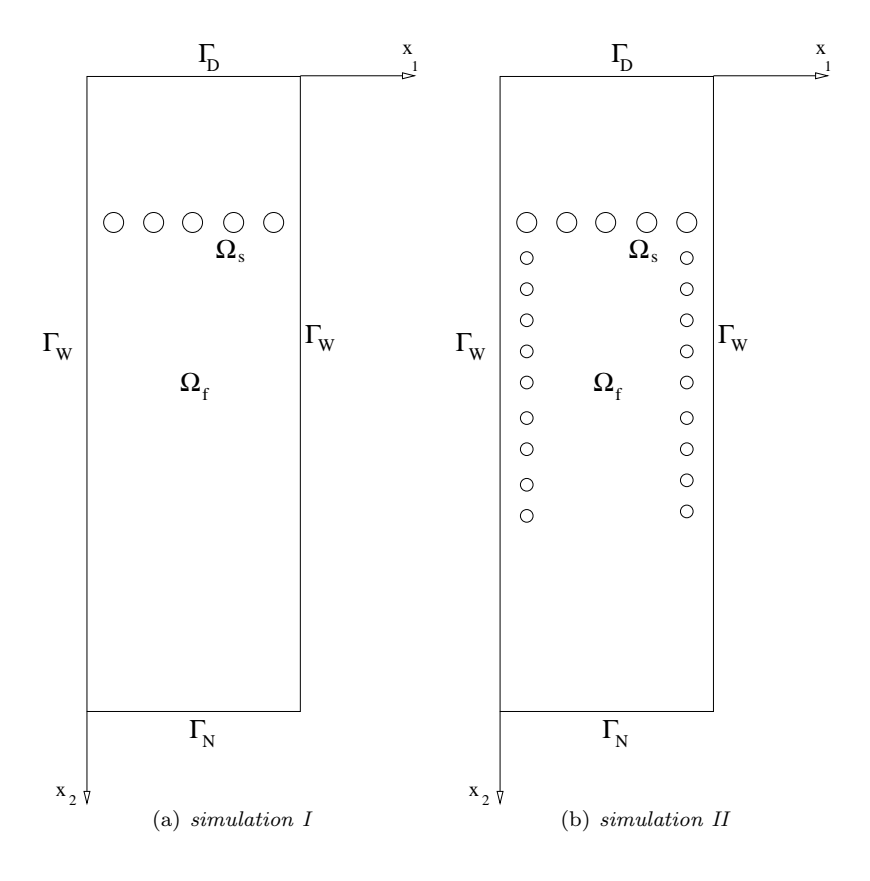


FIGURE 2. Computational domains

events, and thus to enhance the inverse energy cascade phenomenon; the value of the Reynolds number is kept equal to 50000.

In both simulations, the evolutions in time of the velocity (two components), of the vorticity and of the pressure have been recorded at six monitoring points located on the vertical row  $x_1 = 3L/8$  between 5L/16 and 15L/16. These 1D temporal signals have been analyzed and used to compute the energy spectra. The results have been reported in [8, 9].

Numerical results obtained through such DNS can be compared to those obtained in the experiments realized thanks to physical devices by Hamid Kellay in [6]: a soap film in a rectangular channel is disturbed by five big cylinders (as in *simulation I*) or five big cylinders together with two rows of smaller cylinders (as in *simulation II*).

3.2. Mathematical modelization. Let  $\Omega$  be a rectangular bounded domain in  $\mathbb{R}^2$ . The reunion of the five big cylinders and the eighteen small ones is denoted by  $\Omega_s$ . One denotes by  $\Omega_f = \Omega \backslash \overline{\Omega}_s$  the domain for the incompressible fluid in which the NS equations are applied. The boundary of  $\Omega_f$  is defined by  $\partial \Omega_f = \partial \Omega_s \cup \Gamma_D \cup \Gamma_W \cup \Gamma_N$ . A non homogeneous Dirichlet boundary condition is imposed on  $\Gamma_D$  and a no-slip boundary condition on  $\Gamma_W$ . The obstacles are taken into account by a  $L^2$  penalization procedure which consists in adding a mass term in the equations which are now specified on the whole domain  $\Omega$  as in [2].

The tension tensor is denoted by:

$$\sigma(U, p) = \frac{1}{Re} (\nabla U + \nabla U^t) - pI$$
 (22)

where U is the velocity vector, p is the pressure, Re is the Reynolds number and I is the identity operator.

Thus, we are looking for the solution of the following initial boundary value problem:

$$\partial_{t}U + (U \cdot \nabla)U - \operatorname{div}\sigma(U, p) + \frac{1}{K}U = 0 \quad \text{in} \quad \Omega_{T} = \Omega \times (0, T)$$

$$\operatorname{div}U = 0 \quad \text{in} \quad \Omega_{T}$$

$$U(X, 0) = U_{0}(X) \quad \text{in} \quad \Omega$$

$$U = U_{D} \quad \text{on} \quad \Gamma_{D} \times (0, T)$$

$$U = 0 \quad \text{on} \quad \Gamma_{W} \times (0, T)$$

$$\sigma(U, p) \cdot n + \frac{1}{2}(U \cdot n)^{-}(U - U^{ref}) = \sigma(U^{ref}, p^{ref}) \cdot n \quad \text{on} \quad \Gamma_{N}$$

$$(23)$$

where  $U_0$  is the initial datum,  $U_D$  the flow at the beginning of the channel and  $(U^{ref}, p^{ref})$  is a reference flow that is supposed to have the same traction at the exit section than the studied flow [10]. In this NS/Brinkman model, the scalar function K can be considered as the permeability of the porous medium. The permeability is set equal to  $10^{-8}$  in the cylinders, and equal to  $10^{16}$  (should be infinity according to the theory) elsewhere. The NS equations are solved in the fluid, and the Darcy equation is considered in the cylinders [2]. This problem (23) has been theoretically studied in [7]. The numerical solution is based on a finite differences approximation with an explicit second-order scheme in time, an implicit second-order scheme for the pressure and the diffusion terms, and an explicit scheme for the convection terms discretized by a third-order upwind scheme. The simulation is performed on a regular rectangular mesh (1280 × 320) with a multigrid approach. The wavelet or cosine packets transforms have been computed on a square mesh (1024 × 1024).

## 4. Numerical Results.

4.1. **Energy spectrum computation.** The vorticity fields, obtained thanks to the method described in the previous section, for both experiments are represented in Figures 3 and 4. A black and white scale with 256 gray levels has been used. Negative vortices are in black and positive ones in white. A first comment can be made concerning the number and the size of the vortices in both figures. More small vortices, in particular at the end of the channel, can be observed for *Simulation II* due to the action of the nineteen small cylinders. For *Simulation I*, vortices are larger and mainly located in the first half of the channel.

The widely accepted theory of two-dimensional turbulence predicts a direct enstrophy cascade with an energy spectrum which behaves in terms of the frequency range k as  $k^{-3}$  and an inverse energy cascade with a  $k^{-5/3}$  decay.

The study of three-dimensional turbulence theory was initiated by Kolmogorov [22, 23], and then extended to two-dimensional turbulence by Kraichnan [24, 25, 26], Leith [27], and Batchelor [3] (named as KLB theory in the sequel). The theoretical prediction of two inertial ranges is a consequence of both energy and enstrophy conservation laws in the two-dimensional Navier-Stokes (NS) equations. Observing these two ranges in numerical or physical experiments remains a current challenge within the frame of turbulence studies ([5, 31]).

According to Saffman [32], the dominant contribution in the energy spectrum comes from effects resulting from the discontinuities of vorticity. The value of the slope

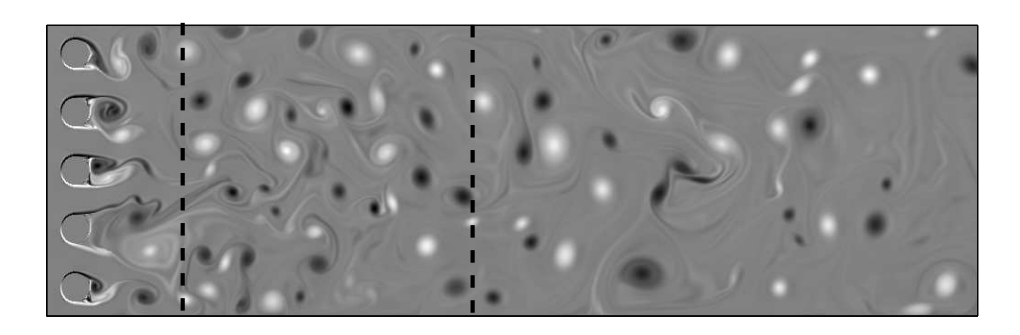


FIGURE 3. Vorticity field for Simulation I

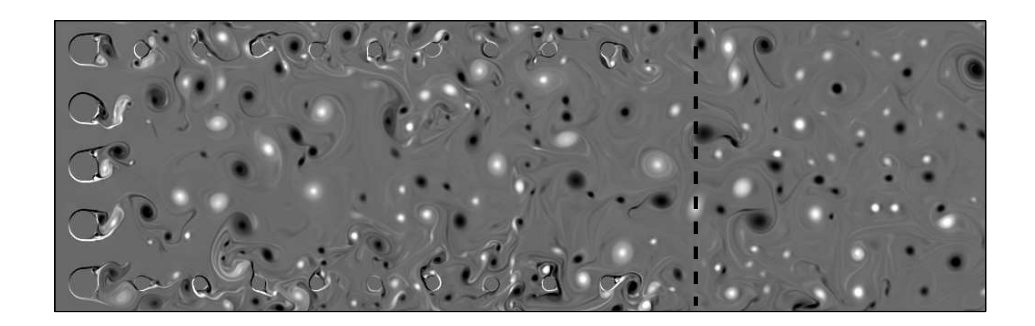


FIGURE 4. Vorticity field for Simulation II

in the representation of the logarithm of the energy spectrum in terms of the logarithm of the wave number is then predicted to be of -4. It follows from the works of KLB that a local cascade of enstrophy from the injection scale to the smaller scales leads to a value of -3 for such a slope. However, the rough value which is obtained by numerical simulations is in general located between these two theoretical values. Vassilicos and Hunt [35] pointed out that accumulating spirals above vortices make the flow more singular, so that the slope is attenuated, down to the value of -5/3. The creation of vorticity filaments leading to these accumulating spirals occurs during the vortices merging process [21]. This process transfers energy to larger scales, thus creating the inverse energy cascade. The theoretical behavior of the energy spectrum in the framework of the KLB theory is depicted in Figure 5. See also [33] for a review on two-dimensional turbulence. Tung, Gkioulekas, and Orlando propose a more general theory based on a double cascades of energy and enstrophy located both upscale and downscale of injection [19, 20, 34]. In their theory, a two dimensional fluid can be written as a linear combination of two distinct homogeneous solutions corresponding to two conservation laws (energy and enstrophy conservation laws) and a particular solution raised by the forcing term and the boundary conditions. The energy spectrum can then be written as:

$$E(k) = E^{(\epsilon)}(k) + E^{(\eta)}(k) + E^{(p)}(k)$$
(24)

where  $E^{(\epsilon)}(k)$  is expected to scale as  $k^{-5/3}$ ,  $E^{(\eta)}(k)$  as  $k^{-3}$  and  $E^{(p)}(k)$  is the contribution of the particular solution.

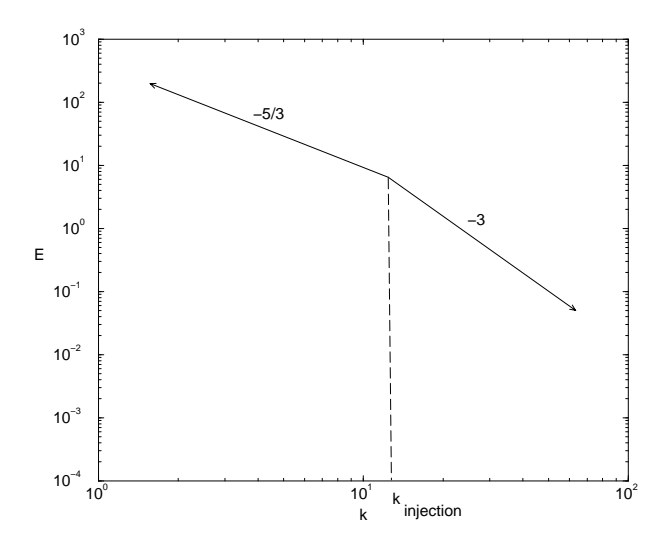


Figure 5. Theoretical spectrum cascades in 2D turbulence

The energy spectra corresponding to both simulations I and II have been computed with a classical two-dimensional Fourier transform applied to a part of the channel. A square containing as many vortices as possible has been selected within each channel for both simulations: in the first half of the channel for Simulation I and in the second half one for Simulation II. The squares are delimited by dashed lines on Figures 3 and 4. The corresponding energy spectra have been computed directly from one 'snapshot' of the flow and have not been time averaged. The spectra, quite noisy, are given in Figure 6. It can be noticed that the second slope, corresponding to the enstrophy cascade, is steeper (-4.5) than the theoretical value (-3). This phenomenon has often been observed in experimental and numerical results.

The problem of the exact determination of the slopes has been addressed in a previous paper [8, 9]. The diameter of the big cylinders being of one tenth of the width of the channel, the main frequency of injection is about  $k \approx 10$ . The diameter of the smaller cylinders in the two vertical arrays is  $\frac{1}{20}$  which corresponds to an injection frequency of  $k \approx 20$ . It can be noticed that the second injection frequency does not seem to interfere in any way in the energy spectrum of Simulation II. A more detailed study of the fluids thanks to wavelet and cosine packets decompositions will allow to determine the effective role of the nineteen small cylinders.

4.2. Wavelet packets decomposition. Daubechies type wavelets [14] have been used to build the packets array and the *entropy* criterion governs the selection process of the best basis. Few tests have been performed in order to chose the best wavelet mother, and to determine how many scales will be necessary to get an efficient representation of the flow. The results are summarized in Tables 2 and 3.

The first remark concerns the difference between  $Simulation\ I$  and  $Simulation\ II$ : the entropy values are bigger for the second simulation. This is due to the presence of more small vortices creating more irregularities in the two-dimensional field. More wavelet coefficients are then requested to represent the signal. For  $Simulation\ I$ , it can be noticed that the gains for the entropy from scale 1 to scale 2 and from

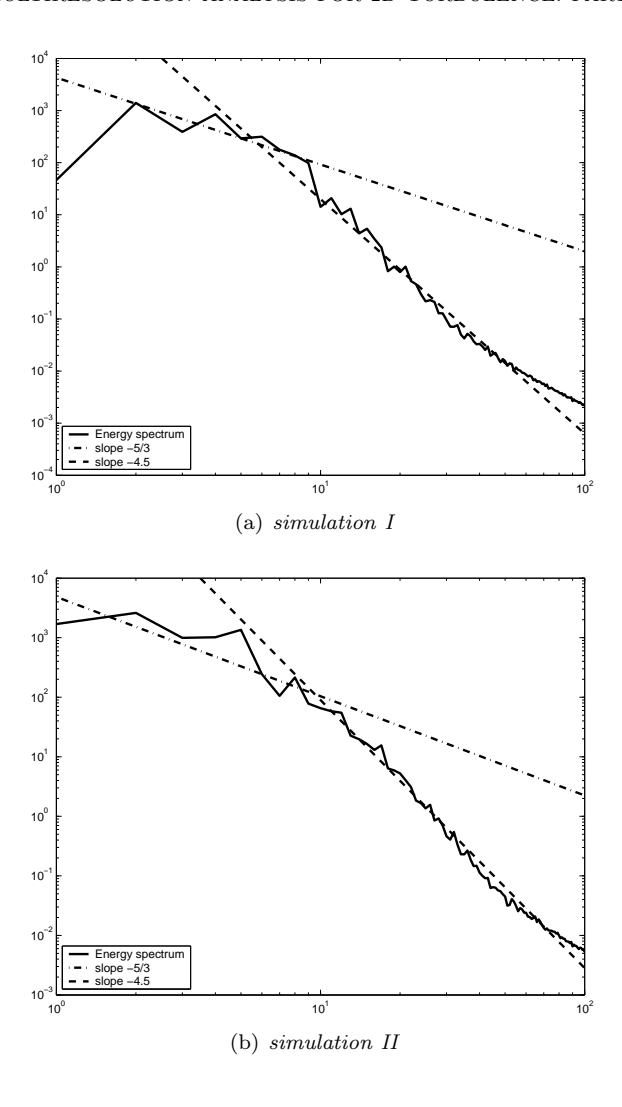


FIGURE 6. Energy spectra

|      | 1     | 2               | 3               | 4              | 5              |
|------|-------|-----------------|-----------------|----------------|----------------|
| D 4  | 57.07 | 48.32 (-15.33%) | 41.69 (-13.72%) | 39.72 (-4.43%) | 39.72 (-)      |
| D 6  | 57.06 | 48.16 (-15.60%) | 41.18 (-14.49%) | 39.58 (-3.89%) | 39.58 (-)      |
| D 8  | 57.09 | 48.18 (-15.61%) | 41.07 (-14.76%) | 40.33 (-1.80%) | 40.31 (-0.05%) |
| D 10 | 57.12 | 48.21 (-15.60%) | 41.00 (-14.96%) | 40.64 (-0.88%) | 40.63 (-0.02%) |
| D 12 | 57.17 | 48.26 (-15.59%) | 41.20 (-14.63%) | 40.45 (-1.82%) | 40.44 (-0.02%) |
| D 14 | 57.22 | 48.43 (-15.36%) | 41.38 (-14.56%) | 40.67 (-1.72%) | 40.67 (-)      |
| D 16 | 57.27 | 48.54 (-15.24%) | 41.54 (-14.42%) | 41.16 (-0.91%) | 41.13 (-0.07%) |

Table 2. Simulation I: Entropy values from scale 1 to 5 for few Daubechies bases ( $gain\ compared\ to\ the\ previous\ scale$ ).

|      | 1     | 2               | 3              | 4              | 5         |
|------|-------|-----------------|----------------|----------------|-----------|
| D 4  | 95.76 | 83.08 (-13.24%) | 78.22 (-5.85%) | 78.22 (-)      | 78.22 (-) |
| D 6  | 95.43 | 82.33 (-13.73%) | 78.21 (-5.00%) | 78.21 (-)      | 78.21 (-) |
| D 8  | 95.40 | 82.10 (-13.94%) | 78.32 (-4.60%) | 78.32 (-)      | 78.32 (-) |
| D 10 | 95.49 | 82.00 (-14.13%) | 77.88 (-5.02%) | 77.88 (-)      | 77.88 (-) |
| D 12 | 95.59 | 82.20 (-14.01%) | 78.24 (-4.82%) | 78.24 (-)      | 78.24 (-) |
| D 14 | 95.65 | 82.64 (-13.60%) | 79.42 (-3.90%) | 79.40 (-0.03%) | 79.40 (-) |
| D 16 | 95.75 | 82.93 (-13.39%) | 80.38 (-3.07%) | 80.35 (-0.04%) | 80.35 (-) |

TABLE 3. Simulation II: Entropy values from scale 1 to 5 for few Daubechies bases (gain compared to the previous scale).

scale 2 to scale 3 are about 15 %. The gains by pursuing the decompositions till scale 4 or more are very weak. So it is not necessary to perform the wavelet packets decomposition over more than 3 scales (at least with the *entropy* criterion). For Simulation II, the decomposition could be stopped after two scales. It has to be reminded that the scale sequence goes from finest scales to coarsest scales. So in the second simulation case (with small structures), it is not necessary to compute approximations on large scales to get a good description of the field.

In brief, a decomposition till scale 3 is necessary for Simulation I and sufficient for Simulation II. So three levels of decomposition will be performed in the sequel for the next computations for both simulations. Concerning the choice of the basis, the few bases which have been tested lead more or less to the same results. But the one which seems to be a little bit better at scale 3 is Daubechies 10. This basis will be chosen for the next computations. One can mention here that the size of the support of a Daubechies 10 function at scale 3 corresponds more or less to the size of the bigger vortex in the vorticity field.

The vorticity fields are then separated into two subfields: one where the wavelet packet coefficients whose moduli are larger than a given threshold  $\epsilon$  and the background subfield where the moduli of the wavelet packet coefficients are smaller than  $\epsilon$ . The subfield with the stronger coefficients corresponds to the coherent structures, and the subfield with the weaker coefficients to the so-called incoherent contributions. The threshold has been chosen empirically, and has been set equal to  $3.10^{-2}$  for a normalized vorticity field. The both subfields corresponding to Simulation I are given in Figures 7 and 8.

The coherent structures are in fact composed by the cores of the vortices and the incoherent contributions are made of the so-called vorticity filaments. In such process, 1088 wavelet packet coefficients have been selected for the coherent field, and the remaining weaker coefficients are all thus in the incoherent field. As it can be checked on Figures 9 and 10, the results obtained for  $Simulation\ II$  are essentially the same .

4.2.1. Energy spectra analysis. The coherent and the incoherent fields, as described in [21], should lead to different energy spectra. They have been computed in the previously defined squares and are given in Figure 11 for Simulation I and Figure 12 for Simulation II.

As expected, the fields constructed from the strong wavelet packet coefficients do not present the same decrease as the fields constructed from the weak wavelet packet coefficients. Slope values around -3 are observed for the coherent contributions,

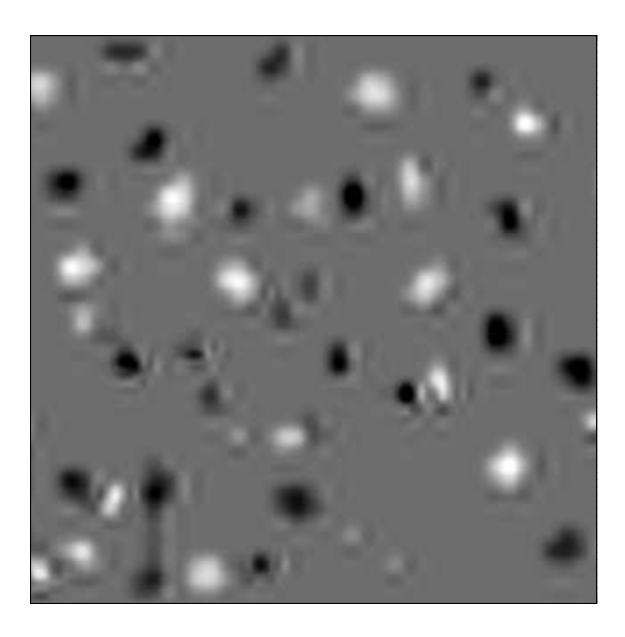


Figure 7. Zoom of the coherent contributions for  $Simulation\ I$ 

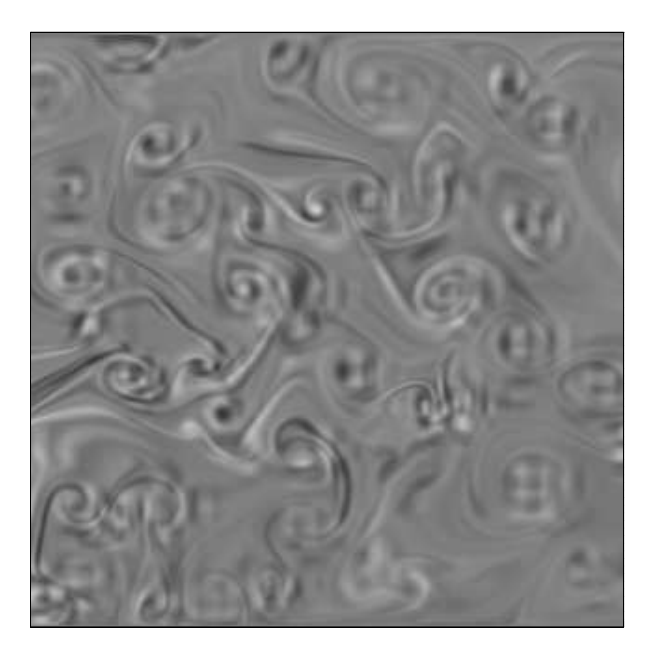


Figure 8. Zoom of the incoherent contributions for  $Simulation\ I$ 

and around -5/3 for the incoherent structures, namely the vorticity filaments. The main difference between  $Simulation\ I$  and II lies in the incoherent contributions field. Indeed the slope decreases like -5/3 till wavenumbers 25-30 for  $Simulation\ II$ , whereas it stops around wavenumber 20 for  $Simulation\ I$ . This can be explained by the fact that the small cylinders create more small vortices around their injection

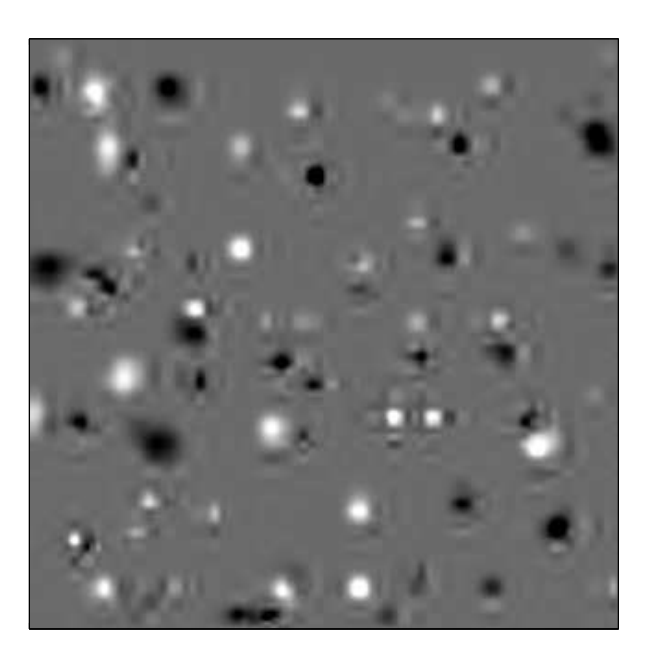


FIGURE 9. Zoom of the coherent contributions for Simulation II

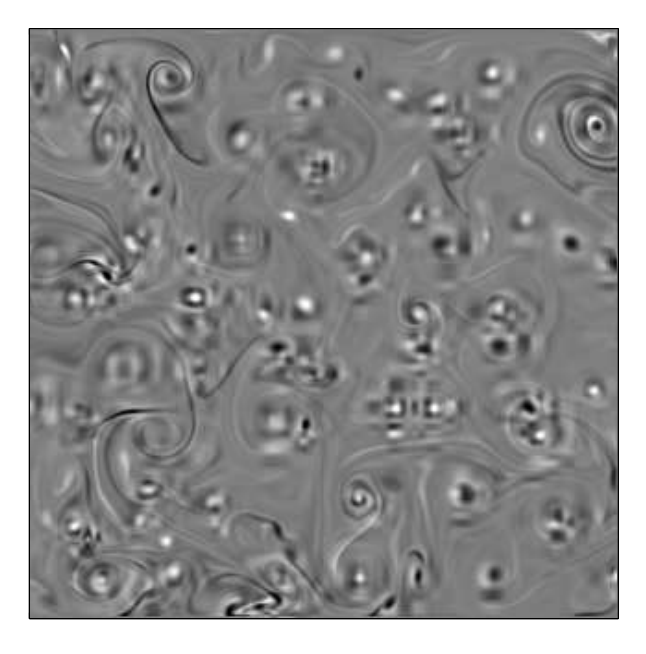


Figure 10. Zoom of the incoherent contributions for Simulation II

scale 20. In a general way, one can say that the fitting with the theoretical values is better for Simulation II than for Simulation I. An unexplained peak around  $k\approx 60$  can be observed in all the reconstructed field energy spectra.

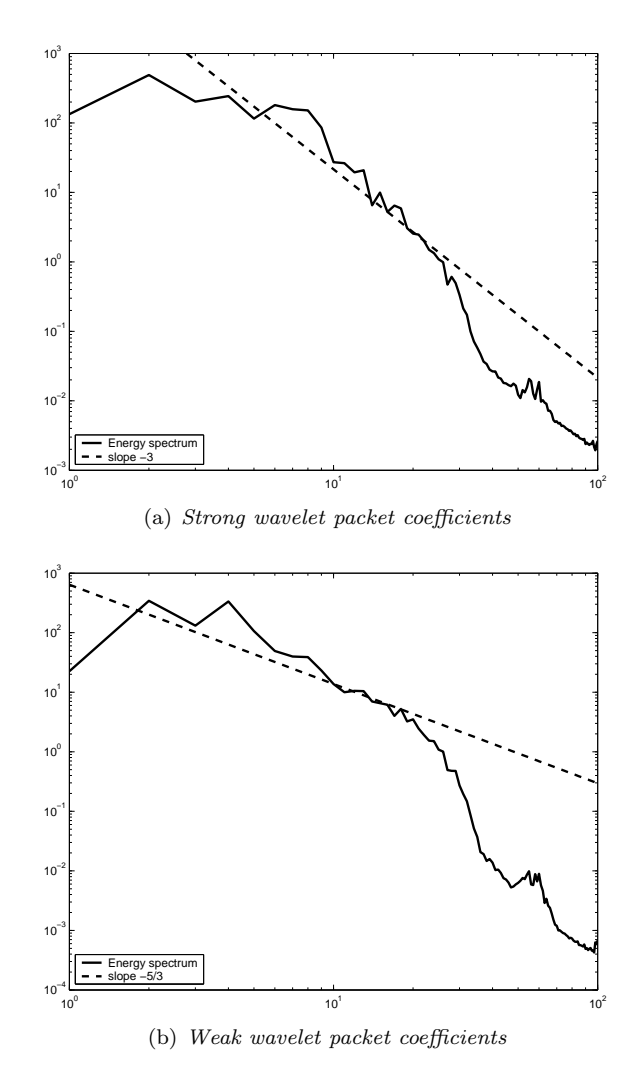


FIGURE 11. Energy spectra for Simulation I

The theoretical value of -5/3 has been explained by Vassilicos and Hunt: accumulating spirals above the vortices make the flow more singular. This theory can be verified by studying in details one vortex thanks to a wavelet packet decomposition. A zoom of the reconstruction with weak wavelet packet coefficients of one vortex from  $Simulation\ I$  is given in Figure 13. The spiral can be easily observed. The same kind of structure can also be detected in  $Simulation\ II$ .

The results presented in this part show that the wavelet packet decomposition is a very well adapted tool for studying two-dimensional turbulence. It can separate two kind of structures, the core of the vortices from the vorticity filaments. The cores lead to an energy spectrum with a slope of about -3, and the filaments to an energy spectrum with a slope of -5/3. The spirals predicted by Vassilicos and Hunt have been clearly observed. These results seem to be in agreement with the theories developed by Tung  $et\ al.$  The inertial ranges where the scale laws are observed lie down on both sides, upscale and downscale, of the injection scale. This

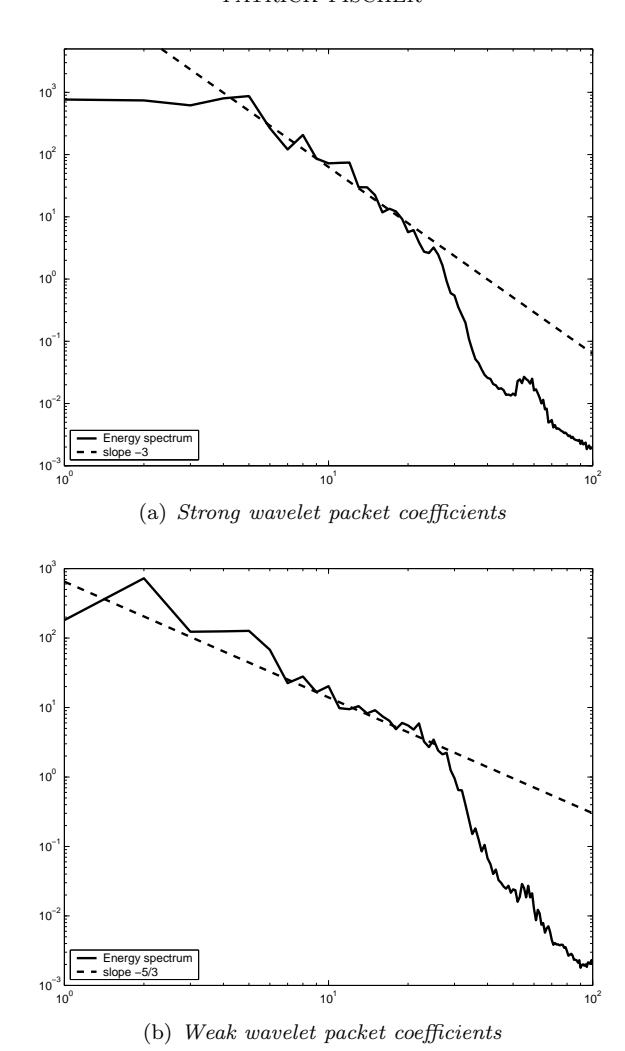


Figure 12. Energy spectra for  $Simulation\ II$ 

could confirm the hypothesis that the both cascades, energy and enstrophy, coexist in the all inertial range of the initial fluid. Another explanation suggested by the reviewer leads to interpret differently these both components. The  $k^{-5/3}$  contribution would correspond to an inverse energy cascade but the  $k^{-3}$  contribution would represent the particular solution associated with the coherent structures. These both explanations will be discussed in the second part of the paper in the light of new numerical and experimental data. In particular, a computation of the energy and enstrophy fluxes could clear this point up. Furthermore, one can notice that the overall spectrum presents a  $k^{-4.5}$  slope in a large part of his range instead of the sum of the two components slopes in contradiction with the theory developed by Tung  $et\ al.$ 

4.3. Cosine packets decomposition. In the one-dimensional case, as mentioned previously, a multiscale version of the local cosine bases is designed using dyadic

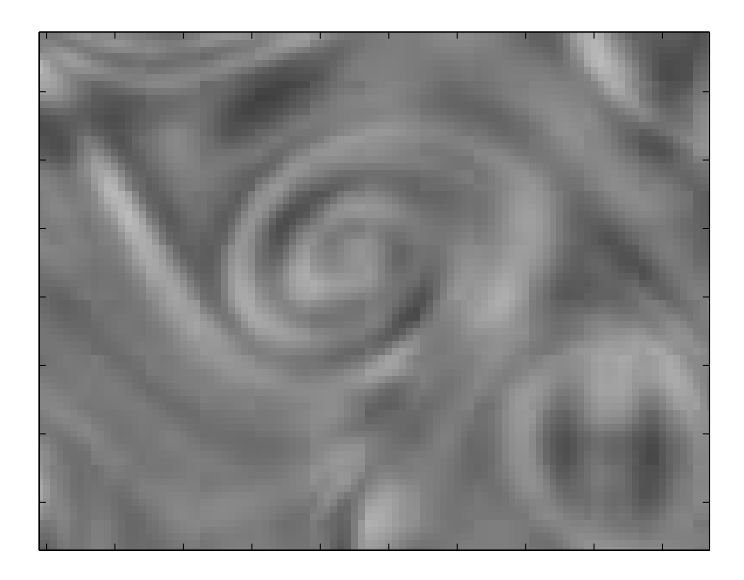


FIGURE 13. Zoom of one selected vortex from the reconstructed field ( $Simulation\ I$ )

partitions of  $\mathbb{R}$ . An initial partition of the real line is refined by breaking the intervals at their midpoints. After such a breaking, a folding is performed at the midpoints. Two methods can be used for this folding: a "fixed folding" in which the radii of the action regions are a fixed  $\epsilon$ , or a "multiple folding" in which the radii of the action regions depend on the level of refinement. In the fixed folding process, the operators used in the refinement will remain disjoint as long as  $2^{-j-1} \geq \epsilon$ where j denotes the level. Thus the number of levels is limited by the choice of  $\epsilon$ . In multiple folding, the maximum radii  $\epsilon_i = 2^{-j-1}$  which keep the folding operator disjoints can be used. Then the number of levels of refinement is, in theory, not limited. Both foldings can be adapted to two-dimensional case, and lead to different results. Entropy values obtained by those methods for both Simulation I and II are reported in Tables 4 and 5. The fixed  $\epsilon$  in the fixed folding process is chosen in order to be allow the computation of all the required levels. The best entropy values are obtained with the fixed folding method and for scale 7. This folding and this scale will be chosen for the next computations. In the same way as in the wavelet packets decomposition, the vorticity fields are then separated into two subfields: one where the cosine packet coefficients whose moduli are larger than a given threshold  $\epsilon = 3.10^{-2}$  and the background subfield where the moduli of the cosine packet coefficients are smaller. The threshold is the same one as the one chosen within the wavelet packets decomposition. The subfields corresponding to strong and weak coefficients and to Simulation I and II are given in Figures 14, 15, 16 and 17.

One can first notice that the figures are very close to those obtained with the wavelet packets decomposition. The same splitting between coherent and incoherent parts has been obtained. That confirms that these components do not depend on the method, but have a real physical meaning. The vorticity filaments and the accumulating spirals (predicted by Vassilicos and Hunt) can be easily observed once the cores of the vortices have been removed with an adapted tool.

| Scale | $Simulation\ I$ | Simulation II   |
|-------|-----------------|-----------------|
| 1     | 56.58           | 111.46          |
| 2     | 50.28 (-11.13%) | 100.87 (-9.50%) |
| 3     | 47.51 (-5.51%)  | 98.00 (-2.85%)  |
| 4     | 45.55 (-4.13%)  | 93.91 (-4.17%)  |
| 5     | 42.76 (-6.13%)  | 88.47 (-5.79%)  |
| 6     | 39.85 (-6.81%)  | 80.91 (-8.55%)  |
| 7     | 38.84 (-2.53%)  | 75.73 (-6.40%)  |
| 8     | 39.84 (+2.57%)  | 75.51 (-0.29%)  |
| 9     | 40.78 (+2.36%)  | 77.44 (+2.56%)  |

TABLE 4. Fixed folding: Entropy values from scale 1 to 9 for Simulation I and Simulation II(gain compared to the previous scale).

| Scale | Simulation I   | Simulation II   |
|-------|----------------|-----------------|
| 1     | 56.49          | 111.51          |
| 2     | 52.10 (-7.77%) | 105.14 (-5.71%) |
| 3     | 50.90 (-2.30%) | 103.74 (-1.33%) |
| 4     | 50.07 (-1.63%) | 101.02 (-2.62%) |
| 5     | 49.45 (-1.24%) | 99.57 (-1.44%)  |
| 6     | 48.60 (-1.72%) | 98.23 (-1.35%)  |
| 7     | 48.11 (-1.01%) | 97.17 (-1.08%)  |
| 8     | 48.00 (-0.23%) | 96.73 (-0.45%)  |
| 9     | 47.98 (-0.04%) | 96.65 (-0.08%)  |

TABLE 5. Multiple folding: Entropy values from scale 1 to 9 for  $Simulation\ I$  and  $Simulation\ II$ (gain compared to the previous scale).

The entropy values corresponding to the cosine packets decomposition are a little bit better (38.84 for  $Simulation\ I$  and 75.73 for  $Simulation\ II$ ) than those corresponding to the wavelet packets method (41 for  $Simulation\ I$  and 77.88 for  $Simulation\ II$ ), but the difference is not really significant.

On the other hand, the pictures obtained thanks to the wavelet packets are better than those obtained thanks to the cosine packets (for instance, in the cosine packets representation of the coherent part, the cores of the vortices have a square shape due to the grid segmentation whereas they have a circular shape closer to the real shape in the wavelet packets representation).

4.3.1. Energy spectra analysis. The coherent and the incoherent fields, as with the wavelet packets decomposition, should lead to different energy spectrum behaviors. They have been computed in the previously defined squares and are given in Figure 18 for Simulation I and Figure 19 for Simulation II.

The results are not as good as the ones obtained with the wavelet packets analysis. This can be easily explained by the fact that the velocity fields from which the spectra are computed are less well described by the cosine packets method than by the wavelet packets method. The artifacts due to the grid segmentation, already

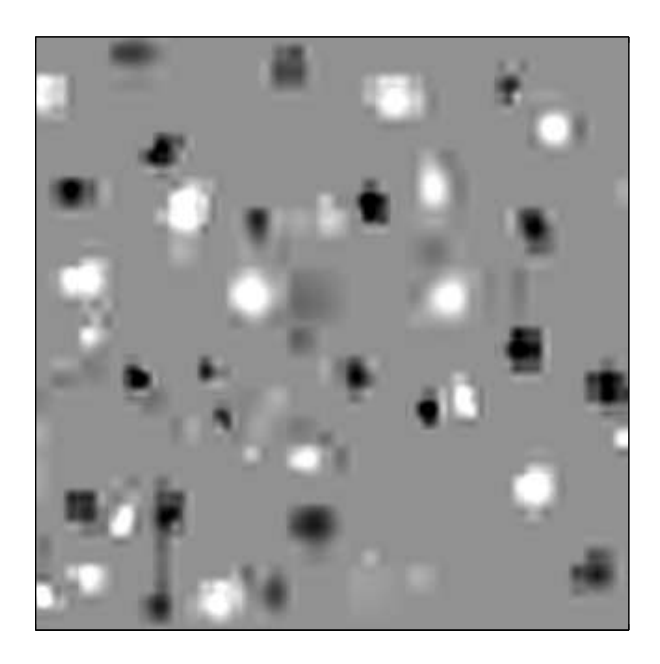


Figure 14. Zoom of the coherent contributions for  $Simulation\ I$ 

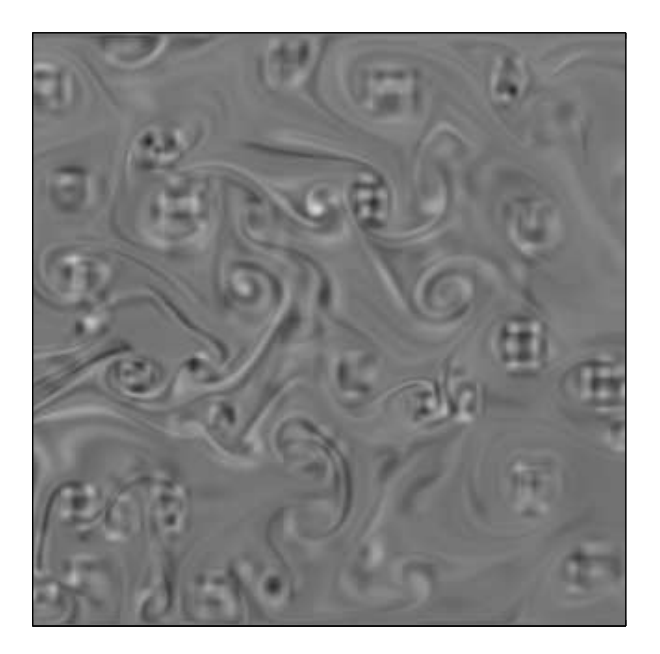


FIGURE 15. Zoom of the incoherent contributions for Simulation I

previously described, are significant in the representation of the velocity field. These artifacts modifies consequently the shape of the energy spectra. In order to apprehend this problem, the velocity fields (corresponding to  $Simulation\ I$ ) constructed from the strong coefficients of the wavelet and cosine packets decompositions are given in Figure 20 and 21.

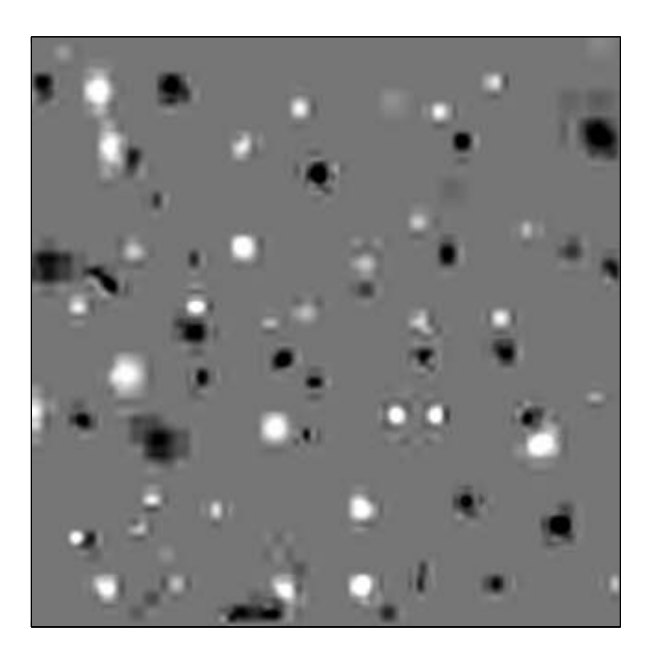


Figure 16. Zoom of the coherent contributions for  $Simulation\ II$ 

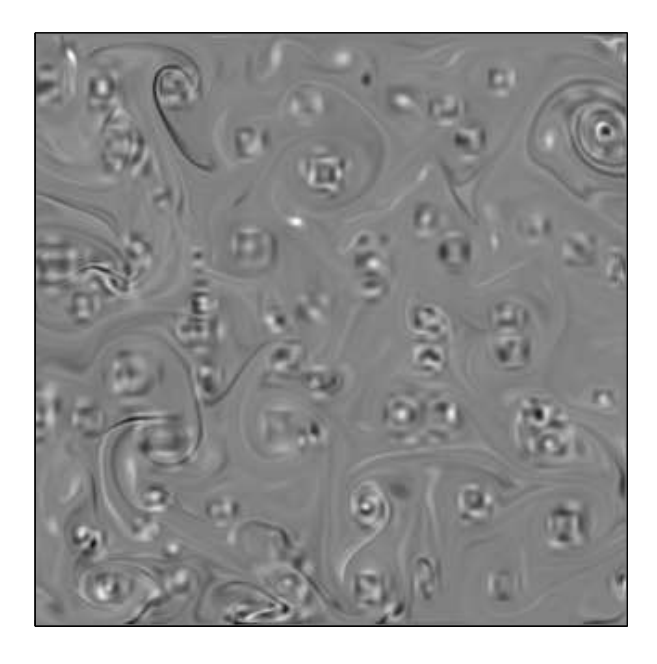


FIGURE 17. Zoom of the incoherent contributions for Simulation II

As can be noticed on Figure 21, the grid structure appears clearly and modify consequently the physical field leading to artifacts in the energy spectrum decomposition. In order to avoid this problem, one may consider the multiple folding method (with  $\epsilon_j=2^{-j-1}$ ) instead of the fixed one. The velocity field (Figure 22)

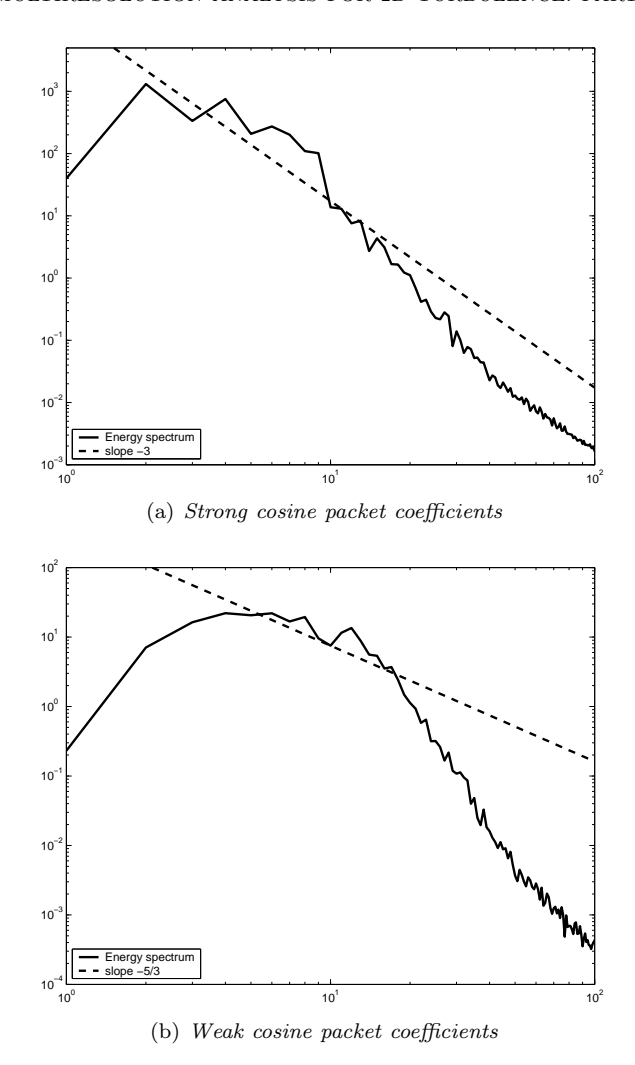


FIGURE 18. Energy spectra for Simulation I

obtained in this way is better, but the corresponding energy spectra are still bad (Figure 23).

So even if the cosine packets decomposition seems to be close to the wavelet packets one, the results are not good.

4.4. Fine grid and time-averaged results: validation of the method. In order to check the validity of the decomposition obtained thanks to the wavelet packet method, the time-averaged spectra for *Simulation II* are given on Figure 24. As expected, the spectra are smoother and are quite close to the theoretical slopes. So one can conclude that this separation in two different components is consistent from a statistical point of view.

Considering now the grid dependence of the results, the computations have been performed on a finer grid  $640 \times 2560$  (instead of  $320 \times 1280$  previously) for one snapshot. The threshold leading to the separation in two components has to be

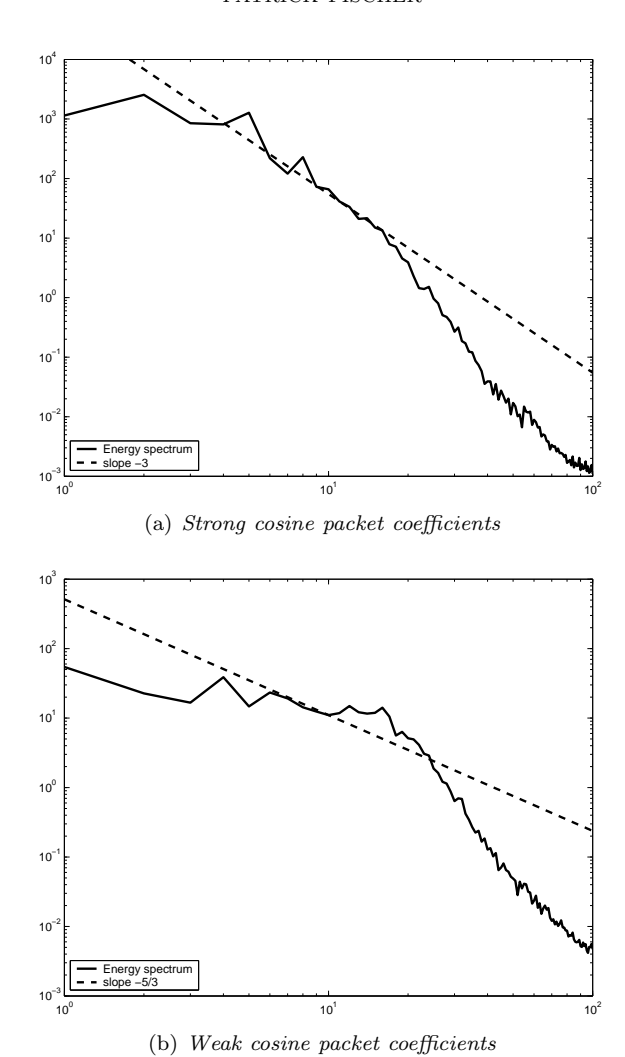


Figure 19. Energy spectra for  $Simulation\ II$ 



FIGURE 20. Velocity field: strong wavelet coefficients for  $Simulation\ I$ 

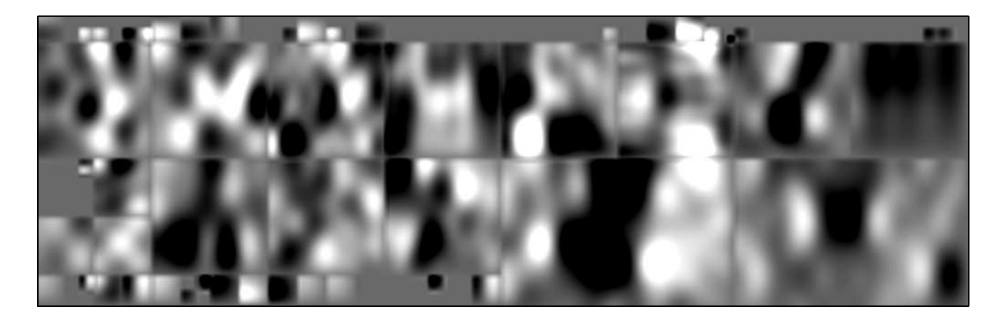


Figure 21. Velocity field: strong cosine coefficients for Simulation I (fixed folding)

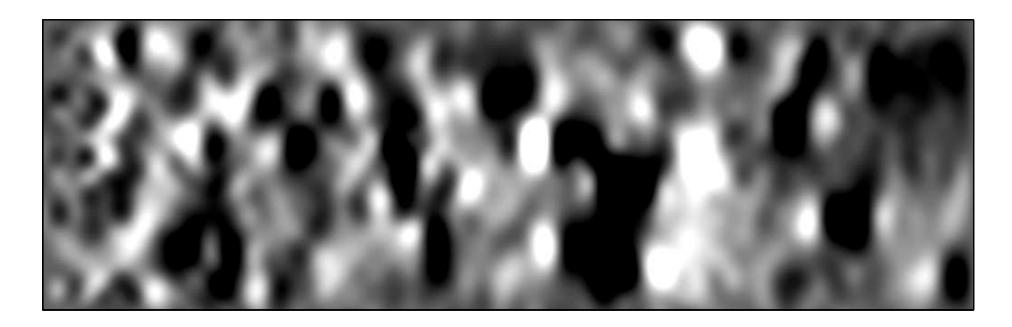


FIGURE 22. Velocity field: strong cosine coefficients for Simulation I (multiple folding)

slightly modified and has been set equal to  $2.10^{-2}$ . The spectra obtained for the both parts are given in Figure 25.

One can remark that the component obtained with the wavelet packet coefficients smaller than the threshold  $2.10^{-2}$  still contains few coefficients describing the core of the vortices. Indeed, a slope close to  $k^{-5/3}$  can be observed in the spectrum for small wavenumbers. In order to remove these coefficients, a threshold slightly smaller has to be used. In this way, the vorticity filaments have been almost completely isolated (Figure 26). A complete discussion about the choice of the threshold will be addressed in the second part of this paper.

5. Conclusions. The aim of the first part of this paper was to compare the efficiency of two decomposition methods, the so-called wavelet and cosine packets, for the analysis of two-dimensional turbulence. The wavelet packets decomposition appears to lead to better results than the ones obtained with the cosine packets method. This method has thus been chosen in order to develop an efficient tool for 2D turbulence analysis. Furthermore, the results seem to be in agreement with the two-dimensional turbulence theory developed by Tung, and could confirm his hypotheses (coexistence of the double cascades of energy and enstrophy in the same range). Nevertheless, the present results don't permit to give an exact physical interpretation for the two components obtained thanks to the wavelet packets decomposition. More results obtained for various kind of numerical computations and soap film experiments will be published in the second part of this paper and

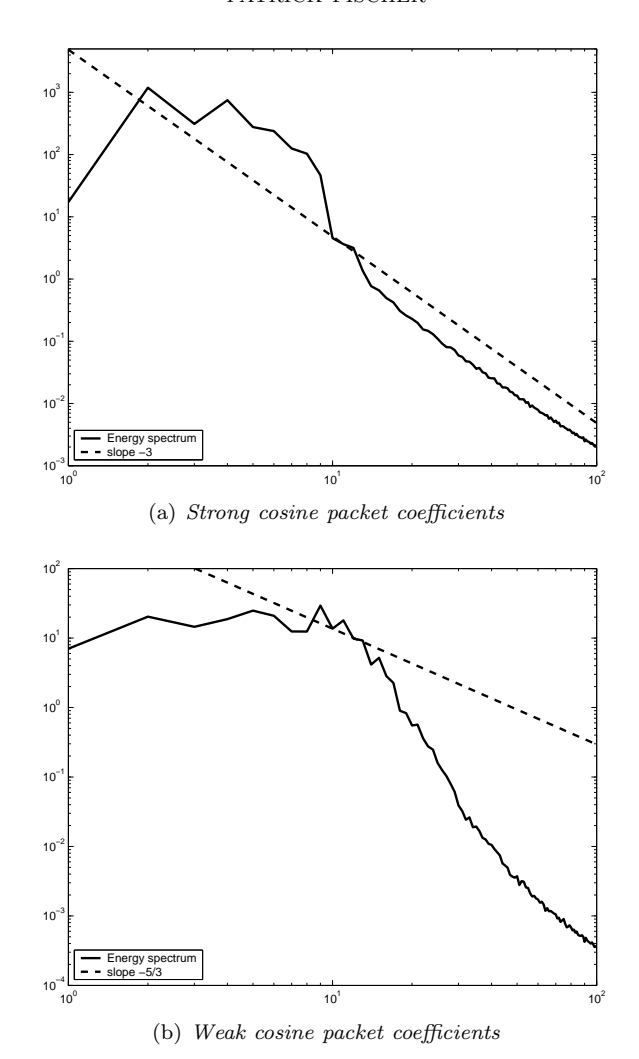


FIGURE 23. Energy spectra for Simulation I (multiple folding)

will give a better insight of the physical problem.

**Acknowledgments.** The author acknowledges with appreciation Professor Bruneau C.H. for useful comments, for providing the data and for reading the manuscript.

## REFERENCES

- Aharoni, G., Averbuch, A., Coifman, R., Israeli, M., Local cosine transform A method for the reduction of the blocking effect, J. Math. Imag. Vis., 3 (1993), 7-38.
- [2] Angot, Ph., Bruneau, C.H., Fabrie, P., A penalization method to take into account obstacles in incompressible viscous flow, Numer. Math., 81 (1999), no. 4, 497-520
- [3] Batchelor, G.K., Computation of the energy spectrum in homogeneous two-dimensional turbulence, Phys.Fluids, 12 (1969), II-233-II-239.

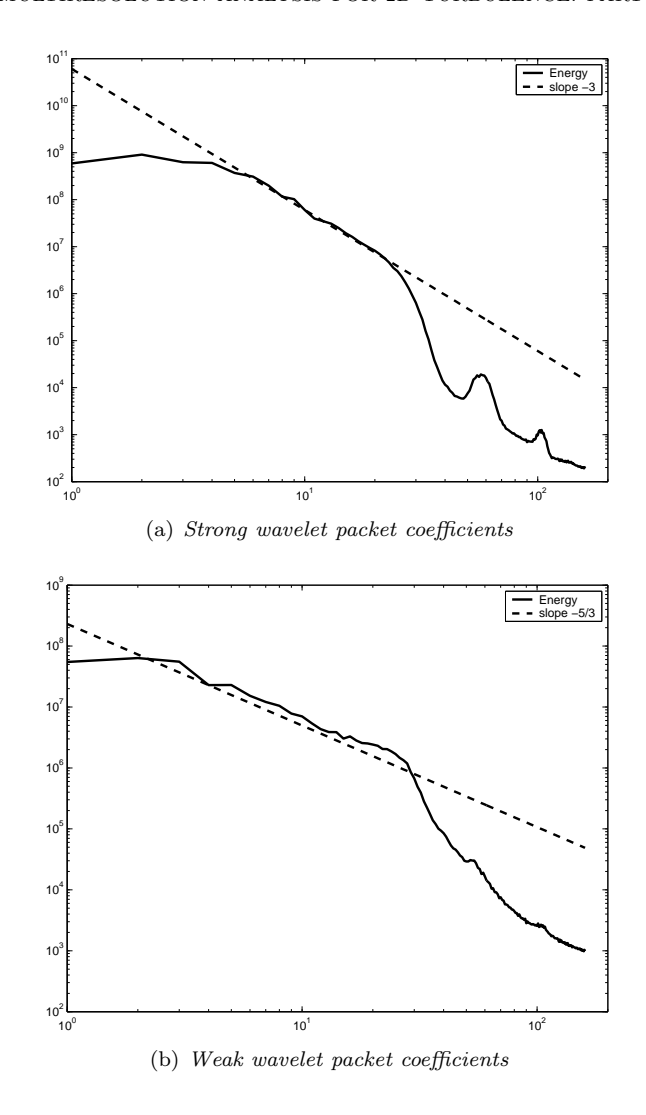


Figure 24. Time-averaged energy spectra for  $Simulation\ II$ 

- [4] Bittner, K., Error estimates and reproduction of polynomials for biorthogonal local trigonometric bases, Appl. Comput. Harmon. Anal., 6 (1999), 75-102.
- [5] Borue, V., Inverse energy cascade in stationary two-dimensional homogeneous turbulence, Phys. Rev. Lett., 72 (1994), 1475-1478.
- [6] Bruneau, C.-H., Greffier, O., Kellay, K., Numerical study of grid turbulence in two dimensions and comparison with experiments on turbulent soap films, Phys. Rev. E, 60 (1999), p: R1162.
- [7] Bruneau, C.-H., Fabrie, P., New efficient boundary conditions for incompressible Navier-Stokes equations: a well-posedness result, RAIRO Modél. Math. Anal. Numér., 30 (1996), no. 7, 815-840.
- [8] Bruneau, C.-H., Fischer, P., Peter, Z., Yger, A., Comparison of numerical methods for the computation of energy spectra in 2D turbulence. Part I: Direct methods, Accepted by Sampling Theory in Signal and Image Processing an International Journal.
- [9] Bruneau, C.-H., Fischer, P., Peter, Z., Yger, A., Comparison of numerical methods for the computation of energy spectra in 2D turbulence. Part II: Adaptative algorithms, Accepted by Sampling Theory in Signal and Image Processing an International Journal.

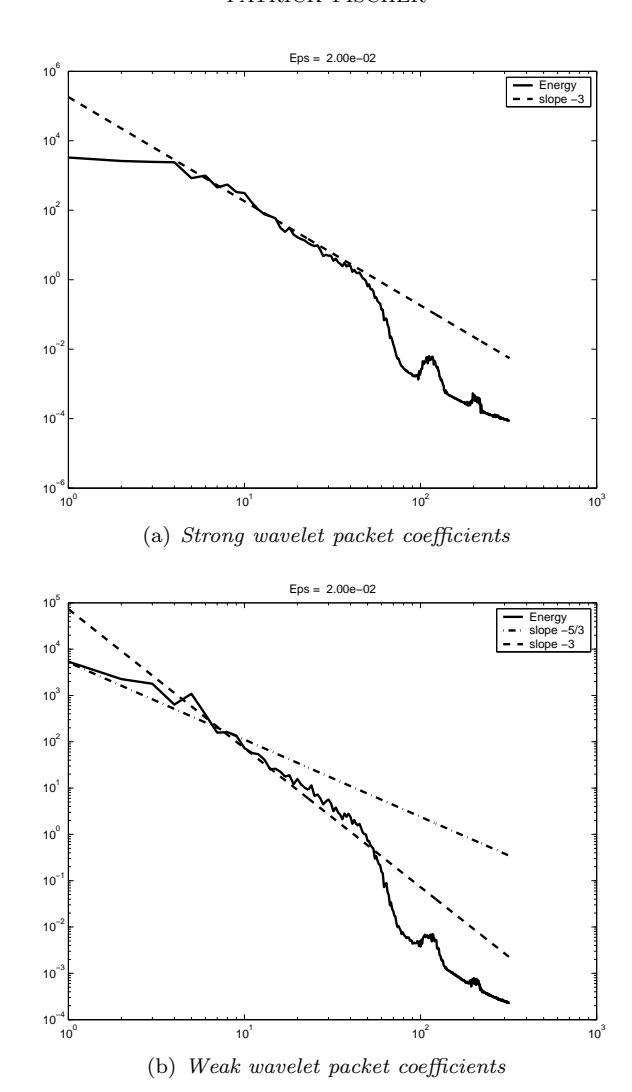


FIGURE 25. Energy spectra for Simulation II on a fine grid

- [10] Bruneau, C.-H., Boundary conditions on artificial frontiers for incompressible and compressible Navier-Stokes equations, M2AN, 34 (2000), no. 2, 303-314.
- [11] Danilov, S., Non-universal features of forced 2D turbulence in the energy and enstrophy ranges, Discrete and Continuous Dynamical Systems Series B, 5 (2005), 67–78.
- [12] Danilov, S., Gurarie, D., Forced two-dimensional turbulence in spectral and physical space, Phys. Rev. E, 63 (2001), 061208.
- [13] Danilov, S., Gurarie, D., Non-universal features of forced two-dimensional turbulence in the energy range, Phys. Rev. E, 63 (2001), 020203.
- [14] Daubechies, I. Orthonormal bases of compactly supported wavelets, Comm. Pure and Appl. Math., 61 (1988), 909-996.
- [15] Donoho, D. WAVELAB802, Software
- [16] Farge, M., Goirand, E., Meyer, Y., Pascal, F., Wickerhauser, M., Improved predictability of two-dimensional turbulent flows using wavelet packet compression Fluid Dynamics Research, 10 (1992), 229-250.

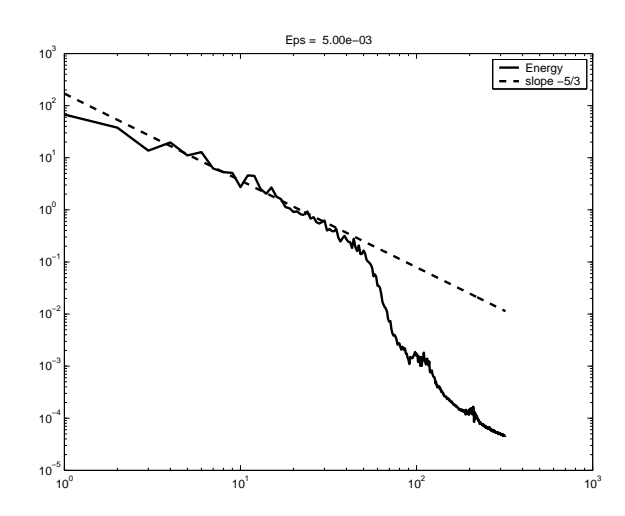


Figure 26. Weak wavelet packet coefficients on a fine grid

- [17] Farge, M., Holschneider, M., Colonna, J.-F., Wavelet analysis of coherent structures in twodimensional turbulent flows in TOPOLOGICAL FLUID MECHANICS (ed. Moffatt H.K. & Tsinober A.), Cambridge University Press.
- [18] Farge, M., Pellegrino, G., Schneider, K., Coherent vortex extraction in 3D turbulent flows using orthogonal wavelets, Phys. Rev. Lett., 87 (2001), no. 5, 45011-45014.
- [19] Gkioulekas E., Tung K. K., On the double cascades of energy and enstrophy in two dimensional turbulence. Part 1. Theoretical formulation, Discrete and Continuous Dynamical Systems B, 5 (2005), 79-102.
- [20] Gkioulekas E., Tung K. K., On the double cascades of energy and enstropy in two dimensional turbulence. Part 2. Approach to the KLB limit and interpretation of experimental evidence, Discrete and Continuous Dynamical Systems B, 5 (2005), 103-124.
- [21] Kevlahan N.K.-R, Farge, M., Vorticity filaments in two-dimensional turbulence: creation, stability and effect, J. Fluid Mech., 346 (1997), 49-76.
- [22] Kolmogorov, A.N., The local structure of turbulence in incompressible viscous fluid for very large Reynolds numbers, Dokl. Akad. Nauk. USSR, 30 (1941), 301-305.
- [23] Kolmogorov, A.N., Dissipation of energy in locally isotropic turbulence, Dokl. Akad. Nauk. USSR, 32 (1941), 16-18.
- [24] Kraichnan, R.H., Inertial ranges transfer in two-dimensional turbulence, Phys. Fluids, 10 (1967), 1417-1423.
- [25] Kraichnan, R.H., Inertial-range transfer in two- and three-dimensional turbulence, J. Fluid Mech., 47 (1971), 525-535.
- [26] Kraichnan, R.H. Montgomery, D., Two-dimensional turbulence, Rep. Prog. Phys., 43 (1980), 547-619.
- [27] Leith, C.E., Diffusion approximation for two dimensional turbulence, Phys. Fluids, 11 (1968), 671-673.
- [28] Mallat, S., Multiresolution Approximation and Wavelet Orthonormal Bases of L<sup>2</sup>(ℝ), Trans. Amer. Math. Soc. 315 (1989), 69-87.
- [29] Malvar, H., Biorthogonal and nonuniform lapped transforms for transform coding, IEEE Trans. Signal Processing, 46 (1998), 1043-1053.
- [30] Matviyenko, G. Optimized local trigonometric bases, Appl. Comput. Harmon. Anal., 3 (1996), 301-323.
- [31] Rutgers, M.A., Forced 2D turbulence: experimental evidence of simultaneous inverse energy and forward enstrophy cascades Phys. Rev. Lett., 81 (1998), 2244-2247.
- [32] Saffman, P.J., Vortex Dynamics, Cambridge University Press, Cambridge, 1995.
- [33] Tabeling, P., Two-dimensional turbulence: a physicist approach Phys. Rep., 362 (2002), 1-62.

- [34] Tung, K. K., Orlando, W. W., The  $k^{-3}$  and  $k^{-5/3}$  energy spectrum of atmospheric turbulence: Quasigeostrophic two-level model simulation, J. Atmos. Sci., **60** (2003), 824-835.
- [35] Vassilicos, J. C., Hunt, J. C., Fractal dimensions and spectra of interfaces with application to turbulence, Proc. R. Soc. Lond. A, 435, 505-534.
- [36] Wickerhauser, M. V., Adapted wavelet analysis from theory to software, A.K. Peters, Wellesley, Massachusetts, 1994.

Received April 2004; revised May 2004; final version August 2004.

 $E ext{-}mail\ address:$  Patrick.Fischer@math.u-bordeaux1.fr